ORIGINAL PAPER

A numerical model for the simulation of debris flow triggering, propagation and arrest

Andrea D'Aniello · Luca Cozzolino · Luigi Cimorelli · Renata Della Morte · Domenico Pianese

Abstract In this paper, it is described the development and the assessment of a 1D numerical procedure for the simulation of debris flow phenomena. The procedure focuses on: (1) the rainfall triggering, and the effects induced on slope stability by both rainfall infiltration and groundwater dynamics; (2) the possible inception of debris flows during the propagation phenomenon itself, due to the actions exerted on the slope by the already triggered flowing masses; (3) the propagation phenomenon over complex topographies; (4) the non-Newtonian internal dissipative processes that develop within the sediment–water mixture; (5) the effects induced by the evolution of the boundaries where the propagation phenomenon occurs; (6) the run-out and arrest phenomena. In order to show the performance and capabilities of the model, the results of its application to an analytic test and to laboratory experimental tests are first analyzed, and finally, the application to a plausible debris flow scenario, taken from a real case study, is discussed.

1 Introduction

The hydrogeological risk is an issue of great importance, due to its detrimental consequences such as human injuries and economical losses related to the damage of buildings, industrial facilities and infrastructures. Among the many forms of hydrogeological

A. D'Aniello (✉) · L. Cimorelli · D. Pianese
Department of Civil, Architectural and Environmental Engineering, University of Naples Federico II, Via Claudio n.21, 80125 Naples, Italy
e-mail: andrea.daniello@unina.it

L. Cozzolino · R. Della Morte
Department of Engineering, University of Naples Parthenope, Centro Direzionale di Napoli – Isola C4, 80143 Naples, Italy

instability phenomena, debris flows are one of the most dangerous, because they are characterized by rapid movements of large masses of soil and water along very steep slopes, with non-homogeneous grain-size distribution (Chen 1988; Takahashi 1991, 2007; Iverson 1997, 2013). Numerous countries are affected by this kind of phenomenon, which is strongly influenced by several factors: (1) the extreme heterogeneity of the geological, geomorphological and hydrogeological structures; (2) the wide range of different micro-climatic conditions, even in neighboring or apparently similar areas, which can trigger the instability of the soil; and (3) the effect of human activities, such as the abandonment of mountainous terrains, the deforestation, the use of invasive agricultural techniques, the opening of borrow pits and the lack of slopes maintenance.

The study of debris flow phenomena is motivated by a number of needs:

- the identification of the causes of the inception, aiming at preventing the onset of such phenomena;
- the identification of the pathways through which these large volumes of material can propagate;
- the evaluation of both the velocities that can be attained by these moving masses and the thrusts that may act on buildings and infrastructures;
- the evaluation of the run-out distances and of the areas susceptible to these forms of instability;
- the risk assessment for human beings, structures, infrastructures and whatever has a value.

Debris flow modeling is a challenging task due to the several complex phenomena involved. In first instance, regarding the triggering phenomenon, distinct mechanisms are reported in the scientific literature: (1) the impact of failed soil masses on stable deposits (Costa and Williams 1984; Di Crescenzo and Santo 2005; Guadagno et al. 2005; Hutchinson and Bhandari 1971; Wang et al. 2003); (2) rainfall infiltration from the ground surface (Guadagno et al. 2005); (3) karst spring from bedrock, as observed for pyroclastic soils in southern Italy (Budetta and de Riso 2004; Cascini et al. 2005; Di Crescenzo and Santo 2005; Guadagno et al. 2005); (4) runoff from bedrock outcrops, as evidenced for shallow landslides in cohesionless soils of the Eastern Italian Alps (Tarolli et al. 2008); and (5) multiple failures in the landslides source areas, as recently evidenced by Cascini et al. (2008).

Numerous 1D and 2D models devoted to mimic the main features of debris flow phenomena have been presented in the scientific field. O'Brien (1986) designed a 1D mudflow model for watershed channels that utilized the Bingham model. Takahashi and Tsujimoto (1985) proposed a 2D finite volume model for debris flows based on a dilatant fluid model coupled with Coulomb flow resistance, and then modified in order to include turbulence (Takahashi and Nakagawa 1989). O'Brien et al. (1993) conceived a 2D finite difference model (FLO-2D) for routing non-Newtonian flood flows on alluvial fans, based on de Saint–Venant equations. An extension of the lumped mass approach has been proposed by Hungr (1995), in which the sliding mass has been represented by a number of blocks contacting each other, free to deform and retaining fixed volumes of material in their descent down a vertically curving path, thus leading to a Lagrangian finite difference solution of the hydrodynamic equations (Potter 1972). On the basis of the integral method (Cunge et al. 1980), a 1D fixed bed debris flow model able to take into account the influence of cross-sectional velocity, density and pressure on debris flow modeling has been proposed by Papa and Pianese (2002). Pianese and Barbiero (2003) presented a 2D finite volume model of the shallow flow type (FVM_2D) able to capture debris flow

propagation over complex topographies with fixed bed devoted to the risk assessment of areas prone to such hazardous phenomena. Mangeney-Castelnau et al. (2003) demonstrated a 2D numerical model of debris avalanches based on depth-averaged de Saint–Venant equations using a finite volume kinetic scheme, in a frame linked to bed topography. Denlinger and Iverson (2004) through a hybrid finite volume/finite element procedure solved a set of 2D depth-averaged momentum and mass conservation equations, following the key elements of the work by Savage and Hutter (1989, 1991), where granular avalanches behave as shallow, isochoric flows of finite volumes of continuous media in which mass and momentum are conserved and shear and normal stresses on internal and bounding surfaces obey the Coulomb friction equation. Pudasaini et al. (2005) demonstrated a shock capturing, total variation diminishing numerical scheme to solve the highly nonlinear equations of their model, which includes the effects of curvature and torsion of the topography in the dynamics of the debris flow, with an explicit influence of the pore pressure distribution. Pastor et al. (2009) developed a 2D smoothed particle hydrodynamics model based on the Biot-Zienkiewicz equations (Biot 1941, 1955; Zienkiewicz et al. 1980, 1999).

These models have often supplied satisfactory results when applied to real-world cases, and a few examples are reported hereinafter: Lin et al. (2005) used FLO-2D for the debris flow simulation of the Chui-Sue River watershed (Taiwan); Cetina et al. (2006) applied both 1D and 2D dam-break flow models, together with FLO-2D, to capture debris flows occurred in 2000 below Stoze (Slovenia); Cosenza et al. (2006) employed the FVM_2D model (Pianese and Barbiero 2003, 2004) with the aim to design concrete structures devoted to the mitigation of debris flow hazard in the Montoro Inferiore area (Southern Italy); Medina et al. (2007) used a finite volume method to solve the 2D shallow water equations in order to mimic the behavior of debris flows in the Northeastern part of the Iberian Peninsula; Sosio et al. (2007) employed the FLO-2D code to replicate the debris flow events on November 2002 of Rossiga Valley (Lombardia, Italy); Quan Luna et al. (2011) tested a 1D model, based on the shallow water assumptions, on a debris flow event that occurred in 2003 in the Faucon torrent (Southern French Alps); in order to reproduce the Sarno-Quindici (Campania, Southern Italy) debris avalanches occurred on May 1998, Cascini et al. (2012) employed a smooth particle hydrodynamics numerical procedure, based on the Biot-Zienkiewicz equations, coupled with both limit equilibrium method and finite element method analysis.

However, several features of debris flow phenomena still constitute an open issue, such as: the entrainment mechanisms, which are able to change significantly the mobility of the flow, through rapid changes of the flow volume and its rheological behavior (Iverson et al. 1997; McDougall and Hungr 2005; Takahashi 2007; Crosta et al. 2008); large grains accumulation at surge fronts, as a result of grain-size segregation and migration within the debris, together with lateral levee formation (Gray and Kokelaar 2010; Iverson 2013); the effects on depositional processes of pore-fluid pressure and friction concentrated at flow margins (Major and Iverson 1999; Major 2000).

Although it is well known that risk assessments of fast-moving flow-like phenomena usually require a 2D approach, in the present work, a 1D approximation is presented. The model described hereinafter cannot be considered a practical tool yet, but rather an attempt to put together into a single numerical procedure several additional complex processes, without the difficulties induced by the 2D aspects of the phenomenon. In order to embody, in the next future, the features described above into a 2D tool, the purpose of the present work is to stress and challenge the potentialities of the 1D model to capture the phenomenon in its entirety.

In this framework, far from wanting to describe all the existing peculiarities of this challenging phenomenon, the attention has been focused on the following features:

- the rainfall triggering, and the effects induced on slope stability by both rainfall infiltration and groundwater dynamics;
- the possible inception of debris flows during the propagation phenomenon itself, due to the actions exerted on the slope by the already triggered flowing masses;
- the propagation phenomenon over complex topographies;
- the non-Newtonian internal dissipative processes that develop within the sediment–water mixture;
- the effects induced by the evolution of the boundaries where the propagation phenomenon occurs;
- the run-out and arrest phenomena.

Regarding its structure, the model consists of the following modules:

- an *infiltration/groundwater module*, which allows to define both the position of the moistening front induced by rainfall infiltration and of the groundwater table, supplying the water pressure distribution in the ground;
- a *slope stability analysis module*, which allows the evaluation of the most probable failure surface along the slope;
- a *propagation module*, which describes the complex phenomenon of debris flow propagation by means of a second-order accurate finite volume method, allowing the evaluation of flow depths and velocities, and the assessment of the morphological changes.

In the remainder of the paper, the abovementioned modules are described in detail: in Sect. 2, the infiltration and groundwater modules are presented; Sect. 3 concerns the description of the slope stability method adopted; and Sects. 4 and 5 are devoted to both the mathematical and numerical characterization of the propagation module. Furthermore, in order to demonstrate the propagation module, in Sect. 6, its applications to an analytical test case (Begnudelli and Rosatti 2011; Cozzolino et al. 2014a), a laboratory dam-break on movable bed (Spinewine and Zech 2007), and a large-scale USGS debris flow experiment (Iverson 2003; Iverson et al. 2010), are presented. Afterward, in Sect. 7, the entire numerical procedure is employed for the simulation of a plausible debris flow scenario involving a slope transect of the Northwestern side of the Posillipo Hill (Naples, Italy), which surrounds the area that, in the next future, will be interested by the construction of the Campegna Station (Mostra-Arsenale section of the Naples underground system, Linea 6). Finally, a section is devoted to the conclusions.

2 Rainfall triggering: infiltration and groundwater modules

Rainfalls have a crucial role in the inception of debris flow triggering mechanisms (Iverson et al. 1997; Iverson 2000), affecting the equilibrium of a slope in different ways. They may cause the rise of the phreatic surface which, in turn, involves an increase of the pore water pressure and a decrease of the shearing resistance of the soil, together with the increase of the soil weight and the increase of destabilizing forces. Moreover, ephemeral springs generated by prolonged rainfalls are able to magnify these effects and in spite of the short period of activity (often shorter than 24 h) and low discharge (10^{-4}–10^{-5} m^3/s) can represent the main triggering mechanism for a debris avalanche (Budetta and de Riso 2004;

Cascini et al. 2012). For this reason, the knowledge of the dynamics of soil water content, infiltration and groundwater processes is of great importance for the prediction of these phenomena.

In the present work, the assumptions that both the hydraulic conductivity and the hydraulic diffusivity are constant and independent of the moisture content are made, and the Horton's model is used in order to evaluate the effects of the infiltration mechanism (Chow et al. 1988). Briefly, the equations of the infiltration module are as follows:

$$f(t) = \begin{cases} P(t) & t < t_p \\ f_\infty + (f_0 - f_\infty)e^{-kt} & t_p \leq t \end{cases} \quad (1)$$

$$F(t) = \begin{cases} \int_0^t P(\tau)d\tau & t < t_p \\ f_\infty t + \dfrac{(f_0 - f_\infty)(1 - e^{-kt})}{k} & t_p \leq t \end{cases} \quad (2)$$

where $P(t)$ is the rainfall rate; f_∞ is the asintotic infiltration capacity; f_0 is the infiltration capacity at time $t = 0$ s; k is a decay coefficient, a constant related to the rapidity of the decrease in infiltration; $f(t)$ is the infiltration rate; $F(t)$ is the total water volume infiltrated per unit of surface area, up to the instant t; t_p is the ponding time, the instant in which the saturation on the surface of the soil is reached.

The groundwater module is based on the hypothesis of steady flow in the vertical (x, z) plane, incompressible fluid, homogeneous and isotropic porous media, no-deformable solid matrix and Darcian regime. As a consequence, the equations on which this module is established are the same utilized to analyze free surface flows in open channels, exception made for the different dissipative processes within the fluid, which are prevalently of viscous nature. In brief, these equations are shown below:

$$\frac{\partial hv}{\partial x} = q \quad (3)$$

$$\frac{dH}{dx} = I - J \quad (4)$$

$$J = \frac{v}{f} \quad (5)$$

where x is the space-independent variable; h is the water depth; v is the fluid profile averaged velocity; q is the uniform discharge influx rate per unit length, supposed orthogonally entering along the path; H is the total head; I is the bed slope; J is the friction slope; and f is the permeability coefficient. The previous equations are solved, for each time interval, by using a classic finite difference method such as the standard step (Chow 1959).

3 Stability module

In order to model the triggering of debris avalanches, a limit equilibrium method (LEM) analysis is carried out by means of the Bishop's method (Bishop 1955). The choice of a LEM analysis is based on the following needs:

- less computational time burdens than those required by more complex analysis, such as finite element method (FEM) analysis, due to the requirement of a model able to run during debris flow propagation. Furthermore, it has been proved (Cascini et al. 2012) that LEM analysis provide factors of safety similar to those given by FEM analysis in the case of geological contexts similar to those examined in the present work (pyroclastic soils, as shown in detail in Sect. 7);
- the possibility to take into account complex topographies together with a stratified soil with different mechanical properties rather than an homogeneous infinite slope (Lambe and Whitman 1968), usually taken as reference for shallow landslides, thus having a tool more suitable for general applications which involve different geological contexts;
- the capability to take into account the simultaneous presence of a moistening front induced by rainfall infiltration and of a groundwater table of any shape.

Among the numerous limit equilibrium methods available in the scientific literature, the Bishop's method has been chosen owing to its proven simplicity, reliability and accuracy. As a matter of fact all the methods based on the global moment equilibrium are more reliable than those ones based on the global force equilibrium: satisfying the global moment equilibrium usually implies the fulfillment of the global force equilibrium, but not vice versa (Bromhead 1986).

Briefly, the Bishop's method assumes that the border of the failure mechanism is defined by a circular surface and imposes a set of hypothesis that allows to reduce the number of the unknowns; otherwise, the equilibrium problem would be underdetermined. The equations on which this model is established are here briefly recalled:

- a vertical force equilibrium equation for each vertical slice in which the potential failure domain is divided

$$Q_i + W_i = N_i' \cos \alpha_i + U_{w,i} \cos \alpha_i - T_i \sin \alpha_i \tag{6}$$

- the Mohr–Coulomb failure criterion for each slice

$$T_i = \frac{c' \Delta s}{F_s \cos \alpha_i} + \frac{W_i \cos \alpha_i - U_{w,i}}{F_s} \tan \varphi' \tag{7}$$

- a global moment equilibrium equation

$$R_i \cdot \sum W_i \sin \alpha_i = R_i \cdot \sum T_i \tag{8}$$

which lead to the following definition of the factor of safety, which is evaluated by means of an iterative approach due to the nonlinearity of the constitutive law:

$$FS = \frac{\sum \left(\frac{Q_i + W_i - U_{w,i} \cos \alpha_i - \frac{c' \Delta s}{F_s \cos \alpha_i}}{\cos \alpha_i - \sin \alpha_i \frac{\tan \varphi'}{FS}} \cdot \tan \varphi' + \frac{c' \Delta s}{\cos \alpha_i} \right)}{\sum \left(P_i \frac{d_P}{R} + W_i \sin \alpha_i + Q_i \frac{d_Q}{R} \right)} \tag{9}$$

where W_i is the weight of the i-th slice; N_i, $U_{w,i}$, and T_i, are the resultant effective normal force, the force exerted by water pressure and the mobilized resultant shear force acting at the base of the i-th slice, respectively; Q_i and P_i are the resultant vertical and horizontal external forces acting on the surface of the i-th slice, respectively; R is the radius of the circular failure surface; d_Q and d_P are the force arms of the resultant vertical and horizontal external forces, respectively; φ' is the effective soil friction angle; c' is the effective

cohesion; Δs is the thickness of the single slice considered; α_i is the angle to the horizontal obtained by the lower contour of the single slice; and FS is the factor of safety.

Equation (9) shows clearly how the presence of a pore water pressure regime in the ground can significantly affect the equilibrium of a slope. For example, a rise of the groundwater table causes an increase of $U_{w,i}$ while the presence of a moistening front propagating from the upper bound of the domain due to rainfall infiltration implies an increase of the soil weight W_i, which, together, concur to a whole decrease of the factor of safety, thus leading to a less stable configuration of the slope.

In the present work, in order to model both the failure stage of a debris avalanche and the possible inception of debris flows during the propagation phenomenon itself, and to reduce the overall computational burden, the stability analysis is accomplished every l time intervals, where l is an user defined value depending on whether the simulation is carried out either under rainfall or under the debris flow propagation, once an appropriate grid of instantaneous rotation centers has been defined, as will be shown in detail in Sect. 7.

4 Propagation module

4.1 Description of the governing equations

The mathematical model used to describe the propagation of 1D debris flows is the following (Cozzolino et al. 2014a; D'Aniello et al. 2014):

$$\frac{\partial \mathbf{U}}{\partial t} + \frac{\partial \mathbf{F}(\mathbf{U})}{\partial x} + \mathbf{H}(\mathbf{U})\frac{\partial \mathbf{U}}{\partial x} = \mathbf{S}(\mathbf{U}) \tag{10}$$

where

$$\mathbf{U} = \begin{bmatrix} h \\ \rho h \\ \rho h u \\ z \end{bmatrix}; \mathbf{F}(\mathbf{U}) = \begin{bmatrix} hu \\ \rho h u \\ p + \rho h u^2 \\ 0 \end{bmatrix}; \mathbf{H}(\mathbf{U}) = \begin{bmatrix} 0 & 0 & 0 & 0 \\ 0 & 0 & 0 & 0 \\ 0 & 0 & 0 & \rho g h \\ 0 & 0 & 0 & 0 \end{bmatrix};$$

$$\mathbf{S}(\mathbf{U}) = \begin{bmatrix} \dfrac{N_b}{c_b} \\ \dfrac{\rho_b N_b}{c_b} \\ -\rho g h S_f \\ -\dfrac{N_b}{c_b} \end{bmatrix} \tag{11}$$

In Eqs. (10) and (11), x and t are the space and time-independent variables, respectively; $\mathbf{U}$ is the vector of the conserved variables; $\mathbf{F}(\mathbf{U})$ is the vector of the fluxes; h is the mixture depth; u is the profile averaged mixture velocity; ρ is the profile averaged mixture density; p is the hydrostatic thrust, defined as $p = 1/2\rho g h^2$; g is the gravity acceleration; z is the bed elevation; N_b is the net volume of sediment transferred from the erodible bed to the flowing water–sediment mixture per unit time and unit bed surface area; S_f is the friction slope; c_b is the sediment concentration in the saturated bed; and ρ_b is the density of the saturated bed.

In the vector Eq. (10), the scalar equations from the first to the third express the conservation equations for volume, mass and momentum of the flowing water–sediment mixture, respectively, while the last scalar equation represents the volume conservation equation for the saturated sediment bed. These equations form a nonlinear system of hyperbolic partial differential equations, which can develop discontinuous solutions also starting from continuous initial conditions (Pianese 1993, 1994). Furthermore, in addition to the discontinuities of the flow field (hydraulic jumps, propagating bores), the bed elevation z can be discontinuous for the presence of artificial and natural bed sills, trenches and deep excavations.

In order to characterize the governing equations, we discard temporarily the source vector $\mathbf{S}(\mathbf{U})$, and rewrite Eq. (10) in quasi-linear form:

$$\frac{\partial \mathbf{U}}{\partial t} + \mathbf{A}(\mathbf{U})\frac{\partial \mathbf{U}}{\partial x} = 0 \qquad (12)$$

where $\mathbf{A} = \mathbf{J} + \mathbf{H}$, and $\mathbf{J} = \partial \mathbf{F}/\partial \mathbf{U}$, is the Jacobian of the fluxes vector.

The matrix $\mathbf{A}$ has four eigenvalues, which are all real and distinct for $u^2 \neq gh$ (Pianese 1993, 1994; Begnudelli and Rosatti 2011). It is easy to see that the term $\rho gh\ \partial z/\partial x$ in the product $\mathbf{A}(\mathbf{U})\partial \mathbf{U}/\partial x$ contains the unknown z, and it is not a source term but it is actually part of the hyperbolic problem: it cannot be recast in divergence form, and then difficulties arise in the definition of the discontinuous solutions of Eq. (10). In order to avoid the restriction of Eq. (10) to the case of continuous bed, and elude the ambiguity introduced by the presence of the non-conservative products, the theory by Dal Maso et al. (1995) is used by Cozzolino et al. (2014a, b, c) for the definition of the weak solutions. In particular, a properly defined vector path ϕ in the space of the conserved variables is chosen between the states $\mathbf{U}_L$ and $\mathbf{U}_R$, to the left and to the right of the generic discontinuity, respectively, obtaining the Generalized Rankine-Hugoniot condition:

$$\xi(\mathbf{U}_R - \mathbf{U}_L) = F(\mathbf{U}_R) - F(\mathbf{U}_L) + S_\phi(\mathbf{U}_L, \mathbf{U}_R) \qquad (13)$$

where ξ is the discontinuity speed, while the subscripts L and R refer to the variables and the fluxes at the left and at the right of the discontinuity, respectively. In Eq. (13), the vector $\mathbf{S}_\phi$ has the form:

$$\mathbf{S}_\phi(\mathbf{U}_L, \mathbf{U}_R) = \begin{bmatrix} 0 \\ 0 \\ P_\phi(\mathbf{U}_L, \mathbf{U}_R) \\ 0 \end{bmatrix} \qquad (14)$$

It can be shown (Cozzolino et al. 2011) that the path ϕ has a clear physical meaning, and its choice coincides with the choice of the pressure distribution acting on the bed discontinuity, while the scalar function P_ϕ represents the force exerted by the flow on the bed discontinuity. Actually, the appearance of the non-conservative products reveals the lack of autonomy of the traditional shallow flow-type mathematical model, which is oversimplified with respect to the physics to be represented when bed discontinuities are present: this lack of autonomy is resolved introducing additional external physical knowledge represented by the path ϕ. In the present work, a hydrostatic pressure distribution is assumed at the bed discontinuities, obtaining the following definition for the scalar function $P_\phi(\mathbf{U}_L, \mathbf{U}_R)$:

- in the case $z_R \geq z_L$

$$\begin{cases} h_L + z_L - z_R > 0, h_R > 0 \rightarrow P_\phi(\mathbf{U}_L, \mathbf{U}_R) = -\dfrac{1}{2} g\rho_L h_L^2 + \dfrac{1}{2} g\rho_L [h_L - (z_R - z_L)]^2 \\ h_L + z_L - z_R \le 0, h_R \le 0 \rightarrow P_\phi(\mathbf{U}_L, \mathbf{U}_R) = -\dfrac{1}{2} g\rho_L h_L^2 \end{cases}$$

$$(15)$$

- instead, in the case $z_R < z_L$

$$\begin{cases} h_R + z_R - z_L > 0, h_L > 0 \rightarrow P_\phi(\mathbf{U}_L, \mathbf{U}_R) = \dfrac{1}{2} g\rho_R h_R^2 - \dfrac{1}{2} g\rho_R [h_R - (z_L - z_R)]^2 \\ h_R + z_R - z_L \le 0, h_L \le 0 \rightarrow P_\phi(\mathbf{U}_L, \mathbf{U}_R) = \dfrac{1}{2} g\rho_R h_R^2 \end{cases}$$

$$(16)$$

For a more detailed characterization of Eq. (10), the interested reader is addressed to Cozzolino et al. (2014a).

4.2 Description of the sediment transport model

In order to take into account the effects of the erosion and deposition of the bed material, the complete Eq. (10) is considered, with source terms defined in Eq. (11). In particular, the net flux of sediment exchanged between the erodible bed and the flowing water–sediment mixture is defined as:

$$N_b = E - D \tag{17}$$

where E and D are the sediment entrainment and deposition fluxes, respectively.

These fluxes are evaluated by means of (Cao et al. 2004):

$$E = \begin{cases} \beta(\vartheta - \vartheta_c)|u|h^{-1}d^{-0.2} \\ 0, \vartheta \le \vartheta_c \end{cases}, \quad D = \alpha c \omega_0 (1 - \alpha c)^m \tag{18}$$

In Eq. (18), ϑ is the Shields' dimensionless shear stress; ϑ_c is a threshold value of the Shields parameter; β is the erosion parameter; d is the sediment equivalent diameter; ω_o is the settling velocity; m is the coefficient of the hindered settling; α is a coefficient for the evaluation of the sediment concentration near the bed; c is the sediment concentration in the flowing mixture; $c_b = 1 - v$ is the sediment concentration in the saturated bed; and v is the bed porosity. The profile averaged density ρ of the flowing mixture, the density ρ_w of the water, the density ρ_s of the sediments and the sediment concentration c are related by $\rho = \rho_w + c(\rho_s - \rho_w)$, while the density ρ_b of the saturated bed and the concentration c_b of the sediment in the saturated bed are related by $\rho_b = \rho_w + c_b(\rho_s - \rho_w)$.

4.3 Description of the rheological model

Debris flows are characterized by wide particle-size distributions, with high concentrations, and then, large particle interactions. In this case, the augmented viscosity and the particle collisions may play significant roles in momentum exchange (Chen 1988). With the aim of taking into account the different dissipative processes within the flowing mixture, the Visco-Plastic-Collisional rheological model is considered. This model is based on the studies made by O'Brien and Julien (1985), O'Brien et al. (1993), who proposed a

physically based quadratic model of the shear stress, that includes yield, viscous, collision and turbulent stress components:

$$\tau = \tau_y + \mu_d \frac{du}{dy} + (\mu_c + \mu_t)\left(\frac{du}{dy}\right)^2 \tag{19}$$

In Eq. (19), the symbols are defined as follows: τ_y is the yield shear stress; μ_d is the dynamic viscosity; $\mu_c = a_1\rho_s\lambda^2 d^2$ is the dispersive parameter, defined by Bagnold; $\mu_t = \rho l_m^2$ is the turbulent parameter, with ρ the mixture density and l_m the mixing length of the mixture. In general, the turbulent parameter is significantly lower than the dispersive one.

Equation (19) can be recast in the following friction-slope form:

$$S_f = S_y + S_v + S_{td} \tag{20}$$

where

$$S_y = \frac{\tau_y}{\gamma_m h}, S_v = \frac{K\eta u}{8\gamma_m h^2}, S_{td} = \frac{n_M^2 u|u|}{h^{4/3}} \tag{21}$$

In Eqs. (20) and (21), the symbols are defined as follows: S_f is the total friction slope; S_y is the yield slope; S_v is the viscous slope; S_{td} is the turbulent-dispersive slope; n_M is the Manning coefficient; K is the viscous resistance parameter; γ_m is the specific weight of the sediment mixture; and η is the fluid viscosity.

5 Proposed numerical procedure

In this work, a second-order extension of the propagation numerical model presented by Cozzolino et al. (2014a) is proposed. A time-splitting procedure is used in order to treat separately the hyperbolic part of the propagation mathematical model and the source terms.

5.1 First-order scheme for the solution of the hyperbolic part: prediction step

Preliminarily, a finite volume scheme first-order accurate in time and space is considered, and the numerical domain is divided into NV finite volumes of length Δx. If $\mathbf{U}_i^n$ is the value, averaged over the i-th cell, of the vector $\mathbf{U}$ at the time level $t^n = n\Delta t$, the predicted solution $\widehat{\mathbf{U}}_i$ of the hyperbolic part of the Eq. (10), assumes the following form:

$$\widehat{\mathbf{U}}_i = \mathbf{U}_i^n - \frac{\Delta t}{\Delta x}\left[\begin{matrix}\mathbf{f}_{HLLC}\left(\mathbf{u}_{i+1/2}^-, \mathbf{u}_{i+1/2}^+\right) - \mathbf{f}_{HLLC}\left(\mathbf{u}_{i-1/2}^-, \mathbf{u}_{i-1/2}^+\right) \\ 0\end{matrix}\right]$$
$$+ \frac{\Delta t}{\Delta x}\left[S_\phi\left(\mathbf{U}_{i+1/2}^-, \mathbf{U}_{i+1/2}^+\right) + S_\phi\left(\mathbf{U}_{i-1/2}^-, \mathbf{U}_{i-1/2}^+\right)\right] \tag{22}$$

In Eq. (22), the states $\mathbf{U}_{i+1/2}^-$ and $\mathbf{U}_{i+1/2}^+$ are reconstructed at the interface $i + 1/2$ between the cells i and $i + 1$ following the generalized hydrostatic reconstruction proposed in Cozzolino et al. (2014a) and are defined as:

$$\begin{cases} \mathbf{U}_{i+1/2}^{-} = \left(h_{i+1/2}^{-} \quad \rho h_{i+1/2}^{-} \quad \rho h u_{i+1/2}^{-} \quad z_{i+1/2} \right)^{T} = \left(\mathbf{u}_{i+1/2}^{-} \quad z_{i+1/2} \right)^{T} \\ \mathbf{U}_{i+1/2}^{+} = \left(h_{i+1/2}^{+} \quad \rho h_{i+1/2}^{+} \quad \rho h u_{i+1/2}^{+} \quad z_{i+1/2} \right)^{T} = \left(\mathbf{u}_{i+1/2}^{+} \quad z_{i+1/2} \right)^{T} \end{cases} \quad (23)$$

where $\mathbf{u} = \left(h \quad \rho h \quad \rho h u \right)^{T}$ is the reduced vector of the conserved variables, and $z_{i+1/2} = \max\left\{ z_i^n, z_{i+1}^n \right\}$.

Regarding the evaluation of the numerical flux f_{HLLC}, an adaptation to variable density shallow flows of the approximate Riemann solver HLLC, originally developed by Toro et al. (1994), has been used (Cozzolino et al. 2014a).

5.2 Second-order extension for the advection part: prediction step

The second-order accuracy in space and time is achieved using a *TVD second-order Runge–Kutta method*. The choice of the method is justified by the following properties of the scheme (Gottlieb and Shu 1998):

- it maintains stability in whatever form, of the Euler forward first-order time stepping, for the high-order discretization, under the Courant-Friedrichs-Lewy (CFL) time-step restriction;
- if an entropy inequality can be proved for the Euler forward, then the same entropy inequality is valid under a high-order TVD time discretization;
- the TVD high-order time discretization is useful not only for TVD spatial discretization, but also for TVB (Total Variation Bounded), or ENO (Essentially Non-Oscillatory), or other types of spatial discretization for hyperbolic problems;
- the low computational storage required;
- it guarantees that each middle stage solution is also TVD.

The TVD second-order Runge–Kutta method is given by:

$$\begin{aligned} \mathbf{U}^{(1)} &= \mathbf{U}^n + \Delta t L(\mathbf{U}^n) \\ \mathbf{U}^{n+1} &= \frac{1}{2}\mathbf{U}^n + \frac{1}{2}\mathbf{U}^{(1)} + \frac{1}{2}\Delta t L\left(\mathbf{U}^{(1)}\right) \end{aligned} \quad (24)$$

where the superscripts n and $n + 1$ refer to the time levels t^n and $t^{n+1} = t^n + \Delta t$, respectively, while L represents the space discretization operator. Variables reconstruction and limitation is needed at each sub-step in order to evaluate the space discretization operator.

The spatial accuracy is achieved by means of piece-wise linear functions (Toro 1999, 2001). A piece-wise linear reconstruction gives:

$$\mathbf{U}_i(x) = \mathbf{U}_i^n + (x - x_i)\frac{\Delta i}{\Delta x}, x \in I_i \quad (25)$$

where $x_i = \left(i - \frac{i}{2} \right)\Delta x$ is the center of the computing cell $I_i = [x_{i-1/2}, x_{i+1/2}]$; Δi is a *slope*, actually a vector difference, which may be found by differencing of neighboring states.

An average between the *intercell slopes* is taken:

$$\Delta i = \frac{1}{2}(1 + \omega)\mathbf{U}_{i-\frac{1}{2}} + \frac{1}{2}(1 - \omega)\mathbf{U}_{i+\frac{1}{2}} \quad (26)$$

where the parameter ω lies in the interval $[-1; 1]$. In general, for most applications, $\omega = 0$ is taken, and in the present work, this approach has been followed.

The TVD constraint is enforced in the reconstruction step by limiting the slopes Δi, in order to avoid the expected spurious oscillations. The *limited slopes* are as follows:

$$\overline{\Delta}_i = \begin{cases} \max\left[0, \min\left(\psi\Delta_{i-\frac{1}{2}}, \Delta_{i+\frac{1}{2}}\right), \min\left(\Delta_{i-\frac{1}{2}}, \psi\Delta_{i+\frac{1}{2}}\right)\right], \Delta_{i+\frac{1}{2}} > 0 \\ \min\left[0, \max\left(\psi\Delta_{i-\frac{1}{2}}, \Delta_{i+\frac{1}{2}}\right), \max\left(\Delta_{i-\frac{1}{2}}, \psi\Delta_{i+\frac{1}{2}}\right)\right], \Delta_{i+\frac{1}{2}} < 0 \end{cases} \tag{27}$$

with

$$\Delta_{i-\frac{1}{2}} = \mathbf{U}_i - \mathbf{U}_{i-1}, \ \Delta_{i+\frac{1}{2}} = \mathbf{U}_{i+1} - \mathbf{U}_i \tag{28}$$

The value $\psi = 1$ reproduces the MINBEE (or MINMOD) flux limiter and $\psi = 2$ reproduces a SUPERBEE limiter. In the present work, $\psi = 1$ has been chosen. It is worth noting that, adopting a MINMOD reconstruction, the only choice which preserves the steady state and the nonnegativity of the flow depth at a wet–dry interface is to work with the quantities h and $h + z$ (Audusse et al. 2004).

Ultimately, at each Runge–Kutta sub-step, the solution is achieved by means of the (22), introducing the following term on the right-hand side of the equation:

$$\mathbf{S}_c\left(\mathbf{U}_{i+1/2}^-, \mathbf{U}_{i-1/2}^+\right) = \begin{bmatrix} 0 & 0 & -0.5g\left(\rho h_{i+1/2}^- + \rho h_{i-1/2}^+\right)\left(z_{i+1/2}^- - z_{i-1/2}^+\right) & 0 \end{bmatrix}^T \tag{29}$$

where $\mathbf{S}_c$ is a central source term introduced in order to satisfy the consistency of the numerical scheme (Audusse et al. 2004).

5.3 Source term treatment: correction step

In order to take into account the friction and erosion–deposition source terms, once that the predicted value $\widehat{\mathbf{U}}_i$ of the conserved variable $\mathbf{U}$ has been found, at each Runge–Kutta sub-step the inhomogeneous problem is solved by means of the Backward Euler method, which is an implicit algorithm:

$$\mathbf{U}^{n+1} = \widehat{\mathbf{U}}_i + \Delta t \mathbf{S}\left(\mathbf{U}^{n+1}\right) \tag{30}$$

where $\mathbf{S}\left(\mathbf{U}^{n+1}\right)$ is the vector source term from Eq. (10). Due to the nonlinearity of the source terms, the Newton–Raphson algorithm is adopted for the solution of Eq. (30), (Cozzolino et al. 2012, 2014a).

In spite of the more computational burden required, the choice of an implicit method instead of an explicit one is motivated by its robustness: as a matter of fact, due to the complexity of the source terms involved in the phenomenon, an explicit source term treatment could have easily induced unexpected oscillations or even instability of the model.

6 Numerical tests

In order to demonstrate the propagation numerical model proposed, a battery of numerical test-cases is considered:

- a synthetic test case (Begnudelli and Rosatti 2011; Cozzolino et al. 2014a) is used to verify the ability of the model to capture analytic solutions on fixed bed with a bed step together with variable density within the fluid;

- a laboratory test case (Spinewine and Zech 2007) is used in order to evaluate the capability of the model to simulate conditions with movable bed;
- the large-scale USGS debris flow experiment (Iverson 2003; Iverson et al. 2010) is reproduced to show the ability of the model to capture the typical features of debris flow during the propagation phenomenon.

6.1 Dam-break over a bed step

In this dam-break test (Begnudelli and Rosatti 2011; Cozzolino et al. 2014a), a horizontal prismatic channel of length $L_c = 200$ m, with the vertical gate located at $x_0 = 100$ m, has been considered. The effects of erosion, deposition and friction have been neglected, and then, the source term $\mathbf{S}(\mathbf{U})$ has been set to zero. The initial conditions, expressed in terms of primitive variables, are defined on the left and on the right of the gate, respectively: $h_L = 5$ m, $u_L = 0$ m/s, $\rho_L = 1,165$ kg/m^3, $z_L = 0$ m, $h_R = 0.9966$ m, $u_R = 0$ m/s, $\rho_R = 1,495$ kg/m^3, $z_R = 1$ m. The numerical solution at time $t = 8$ s has been obtained with $NV = 200$ finite volumes ($\Delta x = 1$ m; $\Delta t = 0.05$ s), considering both the first- and the second-order accurate approximations. The results obtained by using both first- and second-order approximations are represented in Fig. 1 and are compared with the analytical solutions reported in Cozzolino et al. (2014a).

From Fig. 1, it is possible to observe that the numerical method proposed is able to capture with fidelity the contact discontinuity at the bed step, confirming that the hydrostatic pressure distribution at the bed step is enforced, as required by the analytic solution, and that the conservation of mass and volume fluxes at the bed discontinuity are satisfied. In particular, the second-order approximation allows to reduce considerably the differences between the analytical and numerical solutions, especially in correspondence of the shock front.

6.2 Dam-break on movable bed

This test is devoted to verify the capability of the model to cope with movable beds in realistic cases, and for this reason, it has been applied to a laboratory experiment described in Spinewine and Zech (2007). The test is run considering a horizontal rectangular channel of length $L_c = 6$ m, width $b = 0.25$ m, and with the vertical gate located at $x_0 = 3$ m. The bottom is covered on the entire length with a saturated layer of cylindrical PVC pellets, with diameter $d = 3.9$ mm, density $\rho_s = 1,580$ kg/m^3, and porosity $v = 0.42$. At the beginning of the experiment, a layer of tranquil water with depth $h_0 = 0.35$ m is present upstream the gate, and the sudden removal of the gate causes the formation of a dam-break wave that erodes the movable bed. In order to take into account the bed friction and the effects of the erosion and deposition of the bed material, the complete Eq. (10) has been considered, with source terms defined in Eq. (11). The values assumed by the parameters figuring in Eq. (18) are, respectively: $\theta_c = 0.045$; $\beta = 0.0015$ m$^{1.2}$, obtained after a brief calibration, by comparing both the computed water surface and bed elevation profiles with the experimental ones with the aim of finding the best fitting of the data; $\omega_o = 0.15$ m/s; $m = 2.0$; $\alpha = \min\{c_b/c; 2\}$. Regarding the friction slope, the Manning formula has been used with $n_M = 0.02$ s m$^{-1/3}$. Numerical solutions at $t = 0.5$ s, $t = 1$ s and $t = 1.5$ s have been obtained with $NV = 120$ finite volumes ($\Delta x = 0.05$ m; $\Delta t = 0.0025$ s), with reference to the second-
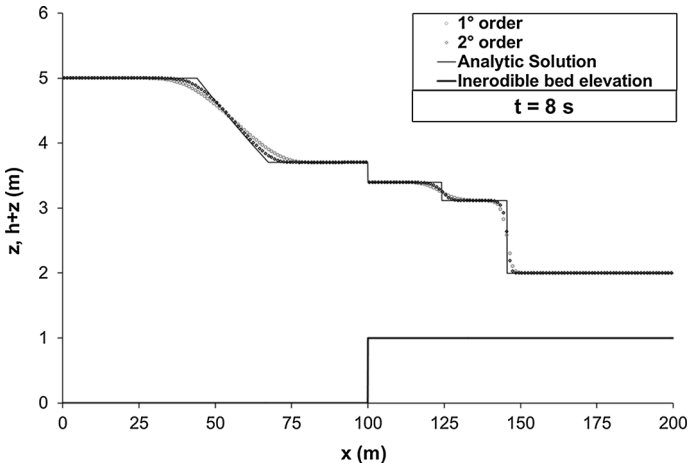
Fig. 1 Dam break over a bed step. Comparison between analytical and numerical solution at time $t = 8$ s
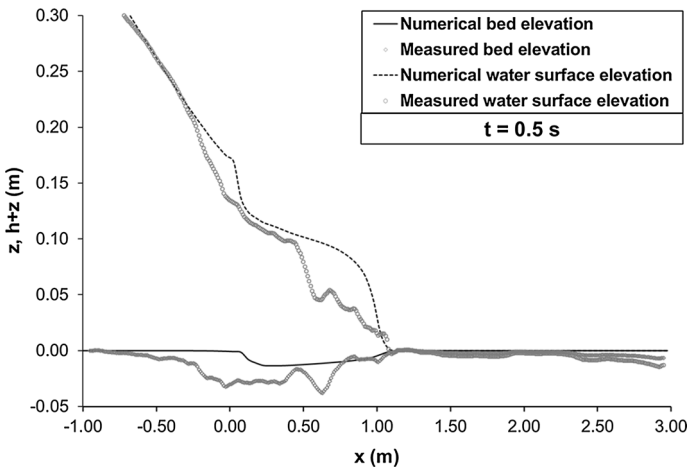

Fig. 2 Dam break on movable bed. Comparison between numerical and laboratory results at time $t = 0.5$ s

order approximation. In order to take into account dry cells, the limit depth has been set to $\varepsilon_h = 10^{-5}$ m. The results obtained are drawn in Figs. 2, 3 and 4.

In Figs. 2, 3 and 4, the comparison between the numerical and experimental results shows a satisfactory agreement between the wave-front celerity positions and an overall agreement between free-surfaces profiles and bottom profiles. A V-shaped longitudinal profile is present close to the dam location due to the change in the sign of the bottom slope downstream the point of maximum excavation, representing a hydraulic jump that is present also in the laboratory experiment by Spinewine and Zech (2007). No ad hoc numerical trick, as small initial flow depth in dry cells, has been used in order to tackle the propagation over dry bed: nonetheless, no negative flow depth has appeared because the Riemann solver used is depth-positivity preserving.
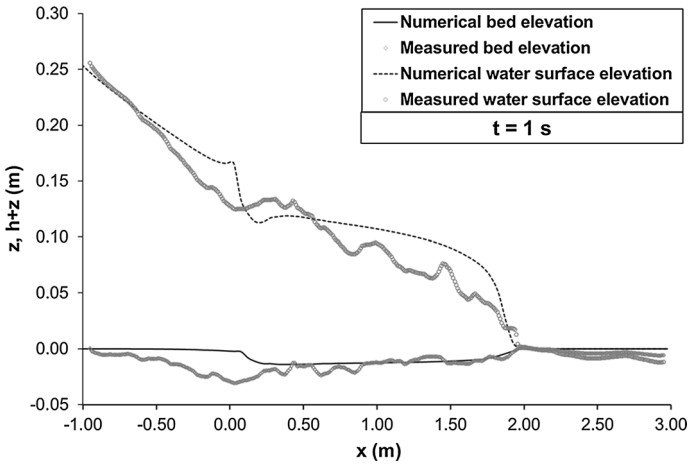
Fig. 3 Dam break on movable bed. Comparison between numerical and laboratory results at time $t = 1$ s
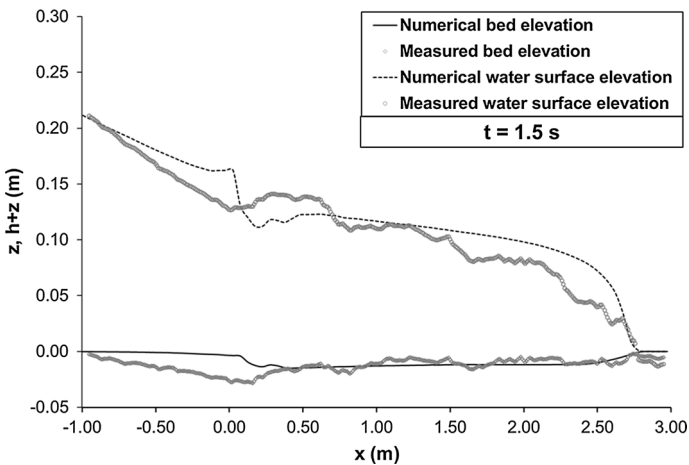
Fig. 4 Dam break on movable bed. Comparison between numerical and laboratory results at time $t = 1.5$ s

6.3 Water-saturated debris flow with a fixed volume: the large-scale USGS experiments

The large-scale USGS experiments (Iverson 2003; Iverson et al. 2010) consist of a wide set of debris flow dam-break tests carried out with different solid materials and water contents.

The tests reproduced in the present work refer to the SGM (sand–gravel–mud) subset experiments on rough bed. The SGM textures consist of 56 % gravel, 37 % sand, and 7 % mud by dry weight, with modal concentrations of grains in the 8–32 mm size classes and secondary modal peaks in the 0.25–0.5 mm size class. In each experiment, the flow is initiated by a sudden release of a wedge-shaped prism of loosely packed, static sediment with 1.9 m height behind the flume head gate. The average prism volume is 9.7 m^3, with sediment porosity of about 0.39, with total water content of about 3.3 m^3 prior flow release.

Moreover, the geotechnical test results give further information about the properties of the water-saturated debris flow slurry, which are summarized hereinafter: $\rho = 2{,}100$ kg/m^3; $\eta = 0.1$ Pa s; $\tau_y = 100$ N/m^2.

Regarding the geometric configuration of the experiment, the USGS debris flow flume is a 95 m long, 2 m wide, rectangular concrete channel that slopes 31° throughout most of its length and flattens at its base to join a run-out surface that slopes 2.5°. Although the steep slope and the width of the channel encourage the development of a nearly 1D flow, the unconfined run-out pad strictly imposes a 2D behavior. Therefore, in order to compare numerical predictions of the proposed 1D second-order accurate propagation model with experimental results, the mean value of the aggregated time series data has been used, with reference to sections located 32 and 66 m below the gate, where the 1D assumption is still verified.

The numerical computation has been carried out considering Eqs. (10), (21), (22), neglecting the erosion and deposition effects. Regarding the remaining parameters used in the course of the simulation, the following values have been assumed: $K = 24$; $n_M = 0.035$ m$^{-1/3}$ s, which is really close to that one used by Paik (2014) for the same test.

The computational domain has been divided in $NV = 742$ finite volumes with $\Delta x = 0.1$ m, while the computational time step has been set to $\Delta t = 0.001$ s. In order to take into account dry cells, the limit depth has been set to $\varepsilon_h = 10^{-4}$ m, and no ad hoc numerical trick, as small initial flow depth in dry cells, has been used in order to capture the propagation over dry bed. The boundary conditions that have been applied are those ones of supercritical outflow.

In Fig. 5, the comparison between the numerical and experimental results shows an overall good agreement. The propagating front position has been well captured at both locations downstream of the gate, and so the arrival time after the flow release, of about 4 and 7 s for each location, respectively. Particular attention must be focused on the arrival time at location 32 m below the gate: Iverson (2013) shows that this arrival time implies that the flow initially attains speeds only slightly less than that of a frictionless body, which theoretically reaches 32 m at $t = 3.56$ s. The large initial flow-front speeds result not from near-zero friction, but instead from a strong downslope thrust (roughly proportional to $-\partial h/\partial x$) that is produced during collapse of the debris as the head-gate opens. As this thrust diminishes, the effects of friction become more apparent.

Regarding the flow thickness, instead, the most discrepancy between numerical results and experimental measurements has been found at location 32 m, where the computed flow thickness has been overestimated by about 50 %. As already observed by Denlinger and Iverson (2001), Paik and Park (2011) and Paik (2014), this discrepancy is attributable to that the depth-averaged models ignore vertical accelerations, which are not negligible in the first instants of a dam-break problem.

7 Case study

In order to stress and challenge the potentialities of the numerical model proposed in the present work, an application of the whole procedure to a plausible debris flow scenario, taken from a real case study, is discussed hereinafter.
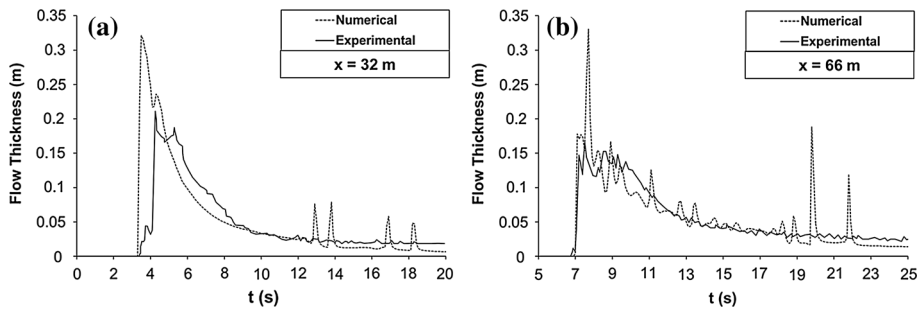
Fig. 5 Large-scale USGS experiment. Comparison between numerical and experimental results at sections **a** x = 32 m, **b** x = 66 m

7.1 Case study framework

The case study area falls in the district of Fuorigrotta (Naples, Italy), in the old Arsenale Militare area located in Campegna Street. It is a flat area limited to the South-East by the Northwestern side of the Posillipo Hill. The plain, of about 20 m above the m.s.l, will be interested by the construction of the Campegna Station (Mostra-Arsenale section of the Naples underground system, Linea 6) and of the railway warehouse (Fig. 6).

The hill–slope reaches a maximum height of about 190 m on the m.s.l., and it is characterized by steep slopes densely covered with vegetation. The area is currently occupied by the old Arsenale Militare (Military Arsenal), where a series of abandoned warehouses lies, close to the hill–slope base. Moreover, different access points to the numerous galleries which extend themselves for tens of meters inside the hill have been noticed, as shown in Fig. 7.

Large areas of the hill–slope are prone to fast-moving flow-like phenomena, as shown in the Landslides Susceptibility Map, Fig. 8, extracted from the Hydrogeological Master Plan, prepared by the Regional Basin Authority of Central Campania. Most of the slope reaches the highest level of susceptibility (P3), while the flat zone at the base of the hill attains the minimum level (P1).

Furthermore, the Landslides Census Map, Fig. 9, arranged by the Regional Basin Authority of Central Campania, shows that the area of interest has already been affected by eight recent landslides: six complex movements (falls with consequent fast-moving flow-like evolution of the phenomenon), and two translational slides.

In the Landslides Risk Map, Fig. 10, extracted from the Hydrogeological Master Plan, a moderate level of risk (R1) is attributed to the area at the base of the slope, while few limited areas are denoted with a high (R3) and very high level (R4) of risk. These areas are characterized by the presence of abandoned sheds and buildings, next to be torn down and replaced by the structures planned for the underground station and the railway warehouse.

If compared to the actual situation, the planned works lead to a change in terms of vulnerability and value at risk. The Landslides Susceptibility Map, with reference to the future interventions, Fig. 11, shows that both the station and the warehouse mostly concern the flat area, in which no risk is expected, while only lead tracks and some sheds reach the base of the slope, thus involving a local change of the risk to a moderate level (R2), due to the high value at risk (E3) and the low level of susceptibility (P1).

Fig. 6 Case study framework. Satellite view (US Department of State Geographer © 2014 Google)
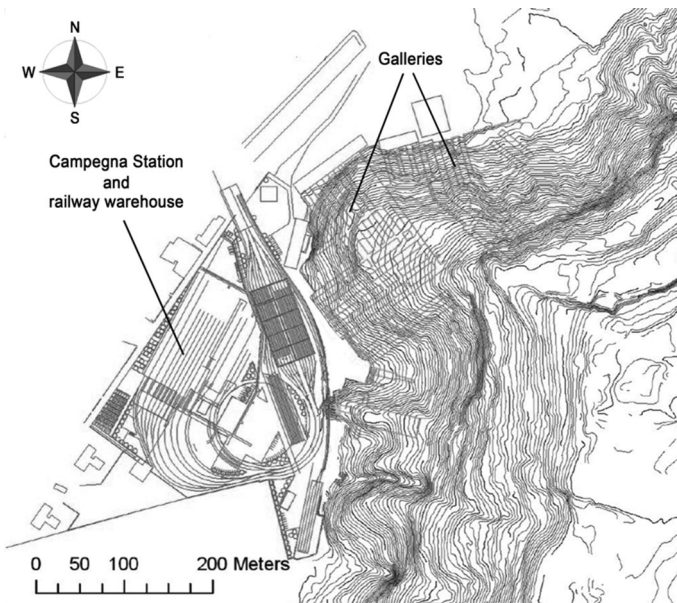

Fig. 7 Case study framework. Schematic representation of the areas of intervention and of the existing system of galleries

Fig. 8 Case study framework. Landslides susceptibility map—hydrogeological master plan (current situation)

7.2 Examined slope transect: a debris flow scenario

In this section, a slope transect of the hill is examined, Fig. 12, with reference to a plausible debris flow scenario. The slope transect under exam is very steep, with slopes ranging from 45 to 80 % with respect to the horizontal.

The stratigraphic sequence that characterizes the site is of volcanic origin and it is composed of the following soil types, listed above, in order from the surface:

- *landfill*;
- *reworked pyroclastic soil*, formed by ashes and pumice due to the eruptions successive to those ones of the Neapolitan Yellow Tuff;
- *loose pyroclastic soil*, consisting of deposited volcanic ashes, volcanic sands and pumice levels formed as a result of the eruptions successive to those ones of the Neapolitan Yellow Tuff;
- *Neapolitan Yellow Tuff*;
- *pyroclastic rocks*, at the base of the Neapolitan Yellow Tuff, consisting of dense white volcanic ashes, with levels of slag and pumice.

Both data and parameters employed in the analysis, and the assumptions made to build the plausible debris flow scenario are discussed hereinafter.
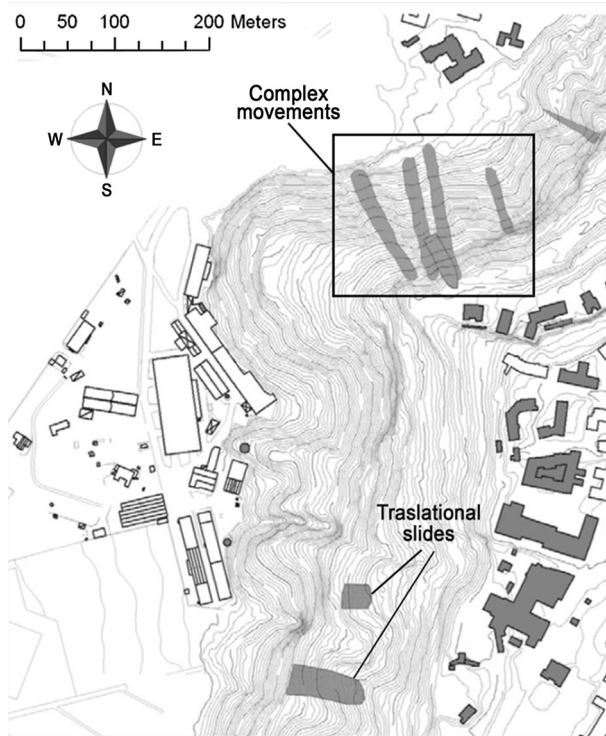
Fig. 9 Case study framework. Landslides census map—hydrogeological master plan (recent landslides)

7.3 Rainfall data

The storm has been deduced from the following expression of the IDF curve (Chow et al. 1988) provided by Rossi and Villani (1995), assuming that the basin in exam falls within the pluviometric sub-area "A1-Litoranea", as identified in the Hydrologic Report, extracted from the Hydrogeological Master Plan, prepared by the Regional Basin Authority of Central Campania:

$$i_{d,T} = \mu_{i_d} K_T = \frac{I_0}{\left(1 + \frac{d}{d_c}\right)^{C+DZ}} \cdot K_T \tag{31}$$

where $i_{d,T}$ (mm/h) is the annual maximum of the rainfall intensity averaged over the duration d (h), having return period T (years); μ_{i_d} (mm/h) is the law with which the expected value of i_d, the annual maximum of the rainfall intensity averaged over the given duration d, varies with the duration itself; $K_T = 3.06$ is the growing factor for the assigned return period, $T = 100$ years, as imposed by the Regional Basin Authority for the risk assessment of areas affected by fast-moving flow-like phenomena; $I_0 = 89.447$mm/h is the average of the annual maximum of the instantaneous rainfall intensity; $d_c = 0.2842$h is the "characteristic" duration; $Z = 100$ m is the hill–slope average elevation above the mean sea level; and $C = 0.758$ and $D = -0.000145$ m^{-1}, are model parameters, calibrated by
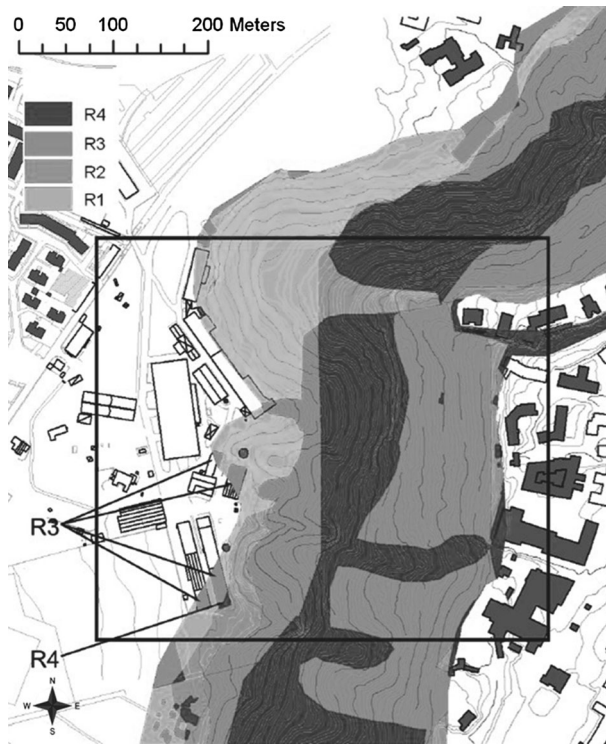
Fig. 10 Case study framework. Landslides risk map—hydrogeological master plan (current situation)

means of the pluviograph data extracted from the hydrological stations located in the area surrounding that one examined in the present work.

7.4 Infiltration and groundwater module data

The parameters of the Horton's model have been evaluated with reference to the soil classification provided by the Soil Conservation Service (1972). In particular, it has been assumed that the soil under exam falls in the B category, "soil with moderately low runoff." In this condition, the infiltration parameters are, respectively: $f_0 = 200$ mm/h; $f_\infty = 12.7$ mm/h; $k = 2$ h^{-1}.

With reference to the groundwater model, a value of the permeability coefficient consistent with the type of soil found along the slope has been estimated equal to 0.00001 m/s (Bilotta et al. 2005).

7.5 Stability module data

In natural conditions, pyroclastic soils exhibit a complex mechanical behavior due to the partial saturation of the pores. Water is present within the pores, and it is subjected to negative pressures (*suction*), which decreases when the saturation degree decreases. The suction gives a cohesive contribution (*apparent cohesion*) to the soil mechanical resistance. A suction increase modifies the stress state of the soil, increasing the effective stress, due to

Fig. 11 Case study framework. Landslides susceptibility map—hydrogeological master plan (future interventions)
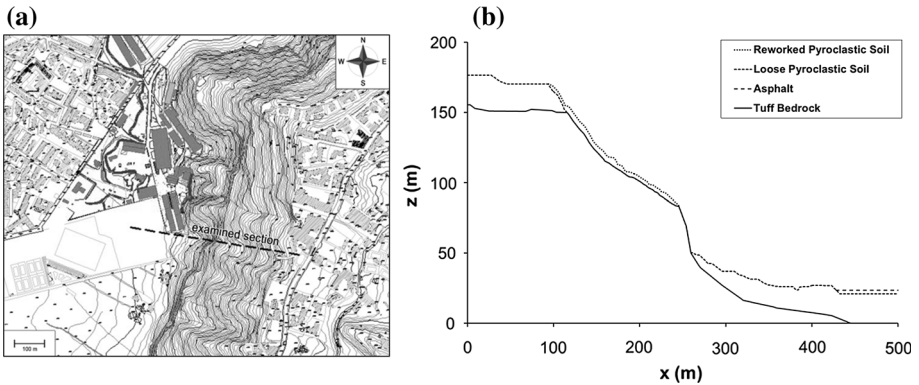

Fig. 12 Examined slope transect: **a** topographic view, **b** examined section

the reciprocal attraction among solid soil particles acted by capillary meniscuses (De Vita et al. 2008).

Unfortunately, the decaying law of the apparent cohesion with the soil water content can be acquired only through a sophisticated and difficult testing. Moreover, neglecting the

apparent cohesion leads to precautionary condition. In this paper, this approach has been followed owing to the lack of information about the soil water retention curve.

The geotechnical parameters assumed for the different layers of soil are listed in Table 1.

These geotechnical parameters have been determined at the former Geotechnical Laboratory of the University of Naples Federico II, Department of Hydraulic, Geotechnical and Environmental Engineering (now Department of Civil, Architectural and Environmental Engineering), using numerous samples taken during in situ inspections.

7.6 Propagation module data

The parameters used to take into account the non-Newtonian internal dissipative process and used in the O'Brien and Julien formula are as follows: $n_M = 0.25$ m$^{-1/3}$ s; $K = 24$; $\eta = 0.574$ Pa s; $\tau_y = 71.69$ N/m^2. These results are based on the rheometric laboratory analyses carried out at the University of Naples Federico II on the pyroclastic deposit samples. The effects of the erosion and deposition of the bed material have been taken into account in the Cao's formula assuming the following parameters: $\beta = 0.0000005$ m$^{1.2}$; $\rho_s = 2{,}600$ kg/m^3; $d = 0.2$ mm; $\vartheta_c = 0.045$; $\omega_0 = 0.000035$ m/s; $m = 2$; $v = 0.58$. The analysis has been performed assuming time step of $\Delta t = 0.001$ s, with a spatial grid of $N = 1{,}840$ cells of length $\Delta x = 0.5$ m. In order to take into account dry cells, the limit depth has been set to $\varepsilon_h = 10^{-4}$ m, and no *ad hoc* numerical trick, as small initial flow depth in dry cells, has been used in order to capture the propagation over dry bed.

7.7 Slope stability and debris flow inception

A preliminary analysis aimed to investigate the stability of the hill–slope in exam, considering the different layers of soil under natural conditions, taking into account only the effective cohesion and soil friction angle, and assuming dry weather. The analysis supplied a minimum factor of safety equal to 1.077 along the slope, which is really close to the critical value of 1.0, thus confirming the slope tendency to instability phenomena.

Successively, the effect of rains has been considered. Past analyses carried out at the University of Naples Federico II have shown that, for geological conditions similar to those ones described above (a layer of *pyroclastic soil* over tuff or calcareous rocks) one of the main causes of debris flow triggering is to be found in the formation of karst springs due to rainfalls of duration of about 32–40 h (Pianese 1999). Therefore, in the first instance, according to Eq. (31), the slope has been subjected to a constant rainfall of duration $d = 40$ h, and the progress of the moistening front has been evaluated at fixed time intervals equal to 2 h. At the end of each time interval, a stability analysis has been performed, in order to evaluate the triggering of the instability phenomenon. In these circumstances, only a slight decrease of the minimum factor of safety along the slope has been detected.

The preceding analysis shows that the rain infiltration through the surface layer is not sufficient to cause the debris flow triggering phenomenon. Then, the existence of one or more ephemeral springs, fed by previous intense rainfall, should be taken into account. On the basis of the field data observed by Cascini et al. (2012) for similar geological contexts, the formation of natural wellsprings with constant discharge equal to $Q = 0.05$ l/s due to the rainfall event has been considered from a given point of the slope ($x = 126$ m; $z = 141.3$ m) to ($x = 245$ m, $z = 83.3$ m), Fig. 12b, and the groundwater analysis has been performed in steady-state conditions, leading to precautionary results. Most of the

Table 1 Geotechnical parameters (Geotechnical Laboratory of the University of Naples Federico II)

Lithotype	γ (kN/m^3)	γ_{dry} (kN/m^3)	γ_{sat} (kN/m^3)	c' (kPa)	φ' (°)
Reworked pyroclastic soil	12.36	10.88	16.55	7	29
Loose pyroclastic soil	14.42	12.75	17.71	12.7	34
Neapolitan yellow tuff	12.02	–	–	1,000	30

γ specific weight in natural conditions, γ_{dry} specific weight in dry conditions, γ_{sat} specific weight in saturated conditions

surface layer of reworked pyroclastic soil is saturated even though the discharge considered is very low. In these conditions, the stability analysis shows that the failure of the pyroclastic layer occurs. The failure domain, shown in Fig. 13, has been obtained as an envelope of all the critical surfaces for which a factor of safety lower than 1 has been found.

7.8 Debris flow propagation

The propagation and run-out analysis have been performed by means of the second-order accurate finite volume scheme described in Sects. 4 and 5, after having defined both the failure domain, whose border turns into the bed over which the debris flow propagation takes place, and, consequently, the volumes susceptible to propagate downstream of the slope, which originate within the failure domain. During the propagation, a stability analysis has been performed at fixed intervals of 1 s in order to evaluate the possible additional failure surfaces induced by either the actions exerted by the unstable masses over the stable ones or by the basis undermining of the surface layer. Figure 14 shows the results of the analysis performed at times $t = 1$ s and $t = 2$ s, when the remaining portions of the pyroclastic layer are triggered due to the actions exerted by the flowing masses.

For the sake of brevity, only few significant snapshots of the numerical results are shown in Fig. 15.

The great destructiveness of a debris flow is clear, especially in the first instants of the propagation phenomenon: in particular, a maximum velocity of about 15.3 m/s has been computed at time 9 s. A few significant plots of both velocity and total thrust profiles are shown at different simulation times in Figs. 16 and 17.

Regarding the arrest process, the stretching of the flow body, the reduction of the flow depth, velocity and of the steepness of the front can be observed. The almost complete arrest of the flowing masses has been attained at a time of about 1,100 s, Fig. 18, and the maximum computed flow depth at rest in the flat non-erodible area is of about 2 m.

The information regarding the total volume per unit meter mobilized is reported in Table 2.

Table 2 shows that in the first instants much of the entrainment is due to the inception of portions of the pyroclastic layer during the propagation of the already flowing masses, and it is of about 148.9 m^3/m, whereas the remaining entrained volume of about 150.9 m^3/m is to be ascribed to the erosional processes of the bed over which the propagation takes place.

Furthermore, an indicative map of the estimate area of invasion has been depicted in Fig. 19.

Although the model is able to capture both the run-out process and the arrest of the flowing masses, it is not capable to reproduce the typical debris flow fan in the depositional
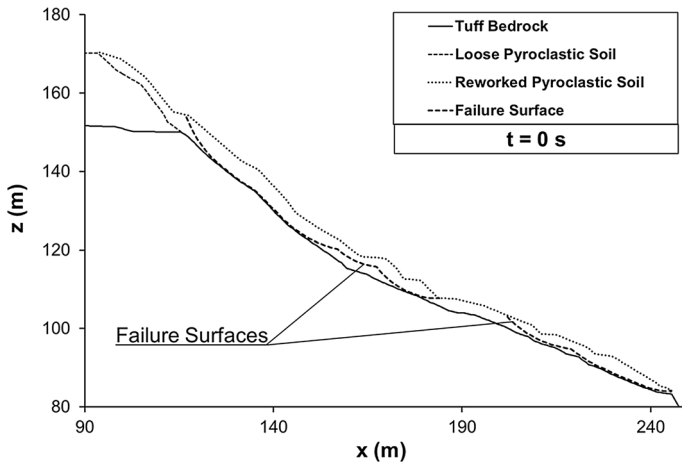
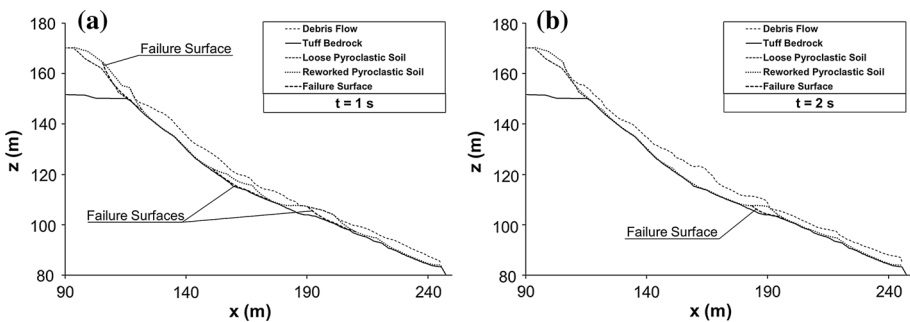Fig. 13 Stability analysis. Initial triggering

Fig. 14 Stability analysis. Additional triggering phenomena during propagation at times **a** $t = 1$ s, **b** $t = 2$ s

area due to the 1D approximation, thus leading to an overestimation of both the run-out distance and the point of arrest.

Finally, it is worth noting that the application of the whole numerical procedure to a realistic debris flow scenario has demonstrated the capability of the model to capture the following features:

- the effects induced on slope stability by both rainfall infiltration and groundwater dynamics;
- the possible inception of debris flows during the propagation phenomenon itself, due to the actions exerted on the slope by the already triggered flowing masses;
- the non-Newtonian internal dissipative processes that develop within the sediment–water mixture;
- the propagation over complex topographies;
- the propagation over dry bed;
- the presence of steep fronts of propagations;
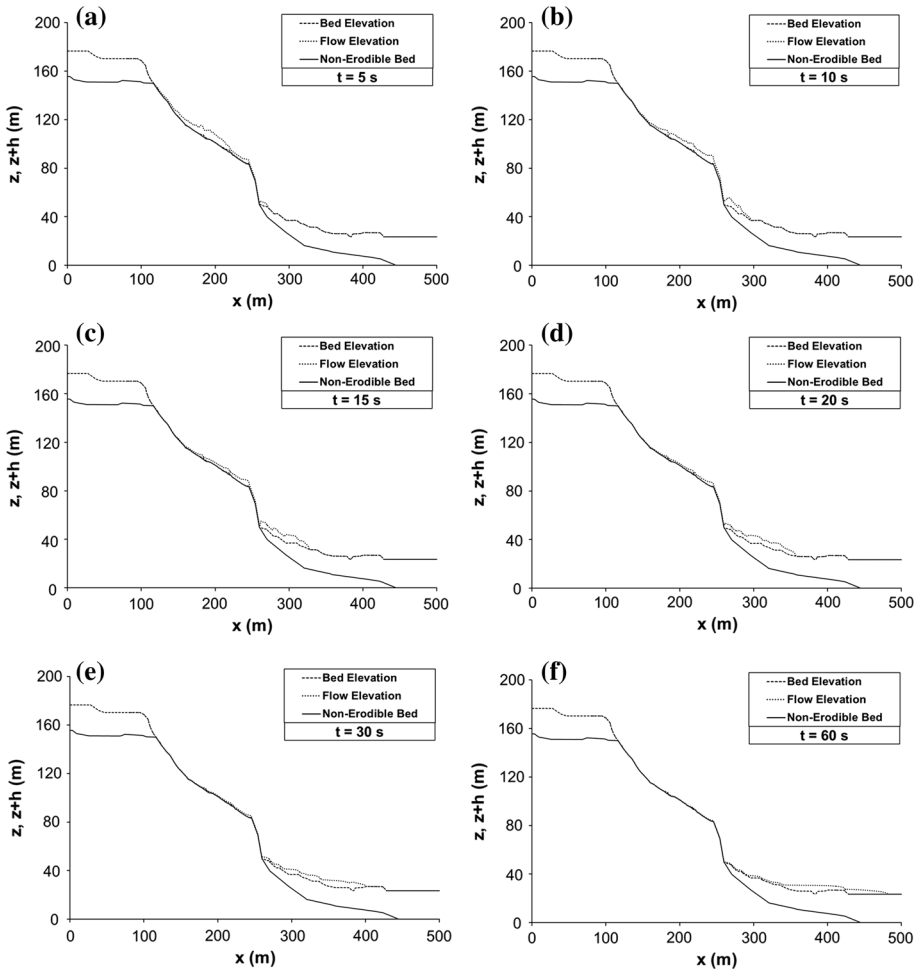- the presence of rapid and sudden subsequent surges;

Fig. 15 Debris flow propagation. Snapshots at time: **a** $t = 5$ s, **b** $t = 10$ s, **c** $t = 15$ s, **d** $t = 20$ s, **e** $t = 30$ s, **f** $t = 60$ s
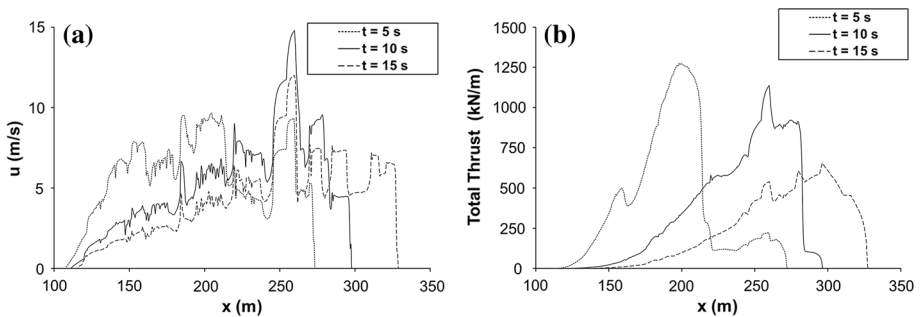

Fig. 16 Debris flow propagation. **a** Mixture velocity, **b** total thrust. Comparison between snapshots at time: $t = 5$ s, $t = 10$ s, $t = 15$ s
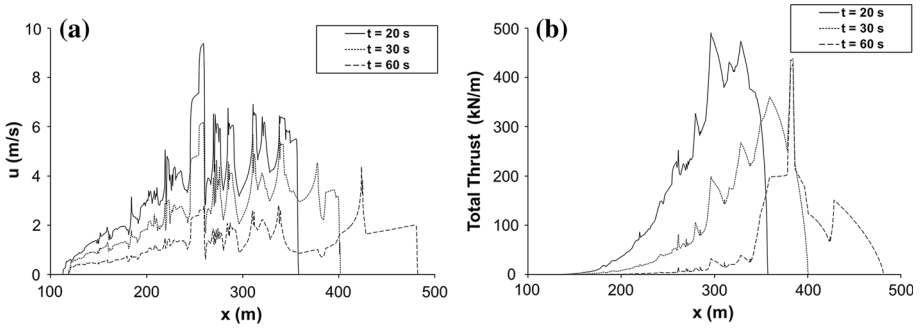
Fig. 17 Debris flow propagation. **a** Mixture velocity, **b** total thrust. Comparison between snapshots at time: $t = 20$ s, $t = 30$ s, $t = 60$ s
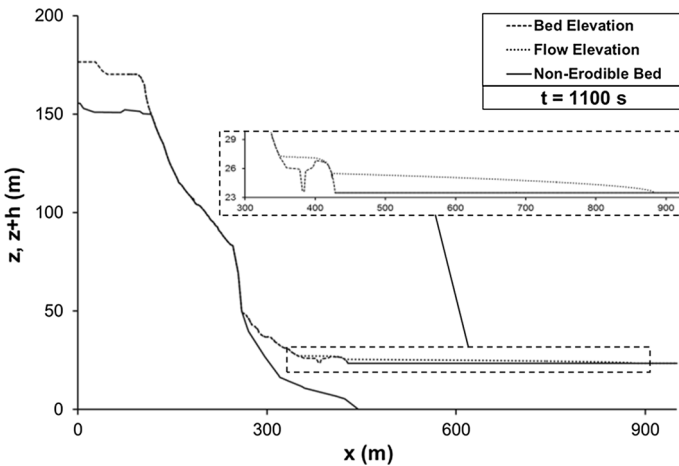

Fig. 18 Debris flow arrest. Snapshot at time $t = 1,100$ s

Table 2 Volume mobilized

Time (s)	Status	Total volume (m³/m)
0	Initial triggering	382.6
1	Triggering during propagation	506.2
2	Triggering during propagation	531.5
1,100	Arrest	682.4

- the interaction between the flow and its solid boundaries;
- the formation of genuine shocks and contact discontinuities due to the presence of geometric discontinuities of the bed;
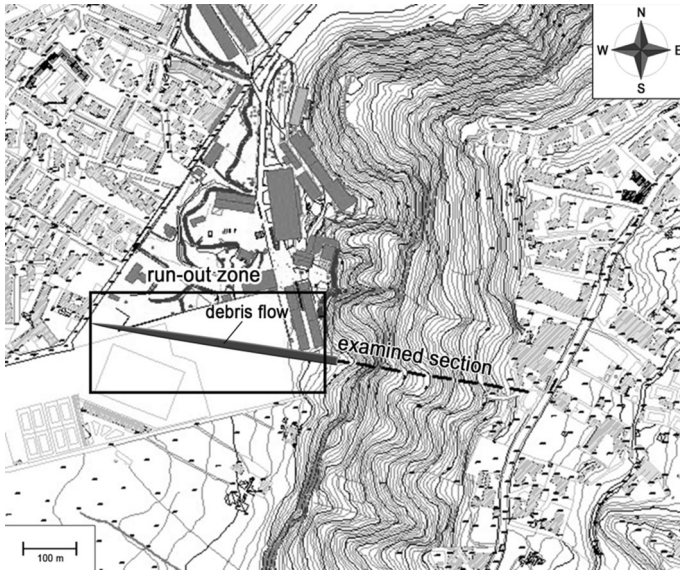- the run-out process and the arrest of the moving masses.

Fig. 19 Indicative area of invasion

8 Conclusions

In this paper, a 1D numerical procedure devoted to the modeling of debris flow phenomena has been proposed. Although its applications to both analytical and experimental tests, and, finally, to a realistic case study, have demonstrated promising and satisfying results, this model cannot be rigorously considered a practical tool yet, but rather an attempt to put together into a single numerical procedure several additional complex processes typical of debris flow phenomena, without incurring in the difficulties induced by the 2D aspects of the phenomenon. Furthermore, a calibration of the parameters is needed. This is achievable only with a proper geotechnical and rheological characterization of the soils in exam. Even though laboratory experiments are useful to get this goal, the comparison of computed results with field measurements is of fundamental importance and cannot be left aside. Indeed, in nature, debris flows can exhibit a behavior strongly different from that one shown during experimental testing: as an example, accounting the presence within the flowing masses of large pieces of heterogeneous materials, such as rocks, trees and vegetation, is a difficult task to deal with. Ultimately, the complexity of the calibration process is enhanced by the lack of field data. As a matter of fact, fast-moving flow-like phenomena are usually sudden and unexpected events: hence, the difficulty of monitoring the phenomenon in its entirety and to gain a full set of field measurements (which involves speeds, thrusts, etc.).

In order to embody, in the next future, the features described above into a 2D model, this work configures itself as a first attempt devoted to challenge the concept itself of a unified framework of modeling, together with the possible implications for the risk assessment of these hazardous phenomena.

References

Audusse E, Bouchut F, Bristeau MO, Klein R, Perthame B (2004) A fast and stable well-balanced scheme with hydrostatic reconstruction for shallow water flows. SIAM J Sci Comput 25(6):2050–2065

Begnudelli L, Rosatti G (2011) Hyperconcentrated 1D shallow flows on fixed bed with geometrical source term due to a bottom step. J Sci Comput 48(1–3):319–332

Bilotta E, Cascini L, Foresta V, Sorbino G (2005) Geotechnical characterization of pyroclastic soils involved in huge flowslides. Geotech Geol Eng 23:365–402

Biot MA (1941) General theory of three-dimensional consolidation. J Appl Phys 12:155–164

Biot MA (1955) Theory of elasticity and consolidation for a porous anisotropic solid. J Appl Phys 26:182–185

Bishop AW (1955) The use of the slip circle in the stability analysis of slopes. Géotechnique 5:7

Bromhead EN (1986) The stability of slopes. Surrey University Press, Glasgow

Budetta P, de Riso R (2004) The mobility of some debris flows in pyroclastic deposits of the northwestern Campanian region (Southern Italy). Bull Eng Geol Environ 63:293–302

Cao Z, Pender G, Wallis S, Carling P (2004) Computational dam-break hydraulics over erodible sediment bed. J Hydraul Eng ASCE 130(7):689–703

Cascini L, Cuomo S, Sorbino G (2005) Flow-like mass movements in pyroclastic soils: remarks on the modelling of triggering mechanisms. Ital Geotech J 4:11–31

Cascini L, Cuomo S, Pastor M, Fernández-Merodo JA (2008) Geomechanical modelling of triggering mechanisms for rainfall-induced triangular shallow landslides of the flowtype. In: Sànchez-Marrè M, Béjar J, Comas J, Rizzoli AE, Guariso G (eds) Proceedings of the iEMSs fourth biennial meeting: international congress on environmental modelling and software (iEMSs 2008). 7–10 July 2008, Barcelona, Spain. International Environmental Modelling and Software Society (iEMSs), Manno, pp 1516–1523

Cascini L, Cuomo S, Pastor M (2012) Inception of debris avalanches: remarks on geomechanical modelling. Landslides. doi:10.1007/s10346-012-0366-0

Cetina M, Rajar R, Hojnik T, Zakrajsek M, Krzyk M, Mikos M (2006) Case study: numerical simulations of debris flows below stoze, Slovenia. J Hydraul Eng ASCE 132(2):121–130

Chen CL (1988) Generalized viscoplastic modeling of debris flow. J Hydraul Eng ASCE 114(3):237–258

Chow VT (1959) Open channel hydraulics. McGraw-Hill Book Company, Inc., New York

Chow VT, Maidment DR, Mays LW (1988) Applied hydrology. McGraw-Hill

Cosenza E, Cozzolino L, Pianese D, Fabbrocino G, Acanfora M (2006) Concrete structures for mitigation of debris-flow hazard in the Montoro Inferiore area, Southern Italy. In Proceedings of 2nd fib congress, June 5–8, 2006, Naples, Italy, paper 19-5, ISBN-10: 88-89972-06-8

Costa JE, Williams GP (1984) Debris-flow dynamics (video tape). US Geological Survey, Open-File Report 84-606

Cozzolino L, Della Morte R, Covelli C, Del Giudice G, Pianese D (2011) Numerical solution of the discontinuous-bottom Shallow-water Equations with hydrostatic pressure distribution at the step. Adv Water Resour 34:1413–1426

Cozzolino L, Della Morte R, Del Giudice G, Palumbo A, Pianese D (2012) A well-balanced spectral volume scheme with the wetting–drying property for the shallow-water equations. J Hydroinform 14(3):745–760

Cozzolino L, Cimorelli L, Covelli C, Della Morte R, Pianese D (2014a) A novel numerical approach for 1D variable density shallow flows over uneven rigid and erodible beds. J Hydraul Eng ASCE 140(3):254–268

Cozzolino L, Cimorelli L, Covelli C, Della Morte R, Pianese D (2014b) Boundary conditions in finite volume schemes for the solution of shallow-water equations: The non-submerged broad-crested weir. J Hydroinf. doi:10.2166/hydro.2014.100

Cozzolino L, Della Morte R, Cimorelli L, Covelli C, Pianese D (2014c) A broad-crested weir boundary condition in finite volume shallow-water numerical models. Proced Eng 70(2014):353–362

Crosta GB, Imposimato S, Roddeman D (2008) Numerical modelling of entrainment/deposition in rock and debris-avalanches. Eng Geol 109(2009):135–145

Cunge JA, Holly FM, Verwey A (1980) Practical aspects of computational river hydraulics. Pitman Advanced Publishing Program, Boston

D'Aniello A, Cozzolino L, Cimorelli L, Covelli C, Della Morte R, Pianese D (2014) One-dimensional simulation of debris-flow inception and propagation. The Third Italian Workshop on Landslides. Procedia Earth Planet Sci 9:112–121. doi:10.1016/j.proeps.2014.06.005

Dal Maso G, LeFloch PG, Murat F (1995) Definition and weak stability of nonconservative products. J Math Pures Appl IX Sèr 74(6):483–548

De Vita P, Angrisani AC, Di Clemente E (2008) Engineering geological properties of the Phlegraean Pozzolan soil (Campania region, Italy) and effect of the suction on the stability of cut slopes. Ital J Eng Geol Environ 2:5–22

Denlinger RP, Iverson RM (2001) Flow variably fluidized granular masses across three-dimensional terrain: 2. Numerical predictions and experimental tests. J Geophys Res 106(1):553–566

Denlinger RP, Iverson RM (2004) Granular avalanches across irregular three-dimensional terrain: 1. Theory and computation. J Geophys Res, 109(F1):1–14

Di Crescenzo G, Santo A (2005) Debris slides-rapid earth flows in the carbonate massifs of the Campania region (Southern Italy): morphological and morphometric data for evaluating triggering susceptibility. Geomorphology 66:255–276

Gottlieb S, Shu CW (1998) Total variation diminishing Runge-Kutta schemes. Math Comput 221(67):73–85

Gray JMNT, Kokelaar BP (2010) Large particle segregation, transport and accumulation in granular free-surface flows. J Fluid Mech 652:105–137

Guadagno FM, Forte R, Revellino P, Fiorillo F, Focareta M (2005) Some aspects of the initiation of debris avalanches in the Campania Region: the role of morphological slope discontinuities and the development of failure. Geomorphology 66:237–254

Hungr O (1995) A model for the runout analysis of rapid flow slides, debris flows, and avalanches. Can Geotech J 32:610–623

Hutchinson JN, Bhandari RK (1971) Undrained loading, a fundamental mechanism of mudflow and other mass movements. Geotechnique 21(4):353–358

Iverson RM (1997) The physics of debris flows. Rev Geophys 35:245–296

Iverson RM (2000) Landslide triggering by rain infiltration. Water Resour Res 36(7):1897–1910

Iverson RM (2003) The debris-flow myth. In: Chen CL, Rickenmann D (eds) Debris flow mechanics and mitigation conference. Mills Press, Davos, pp 303–314

Iverson RM (2013) Mechanics of debris flows and rock avalanches. In: Joseph H, Fernando S (eds) Handbook of environmental fluid dynamics, vol One. CRC Press/Taylor and Francis Group, LLC, pp 573–587

Iverson RM, Reid ME, LaHusen RG (1997) Debris-flow mobilization from landslides. Annu Rev Earth Planet Sci 25:85–138

Iverson RM, Logan M, LaHusen RG, Berti M (2010) The perfect debris flow? Aggregated results from 28 large-scale experiments. J Geophys Res 115:F03005

Lambe TW, Whitman RV (1968) Soil mechanics. Wiley, New York

Lin M-L, Wang K-L, Huang J-J (2005) Debris flow run off simulation and verification: case study of Chen-You-Lan watershed, Taiwan. EGU NHESS 5:439–445

Major JJ (2000) Gravity-driven consolidation of granular slurries: implications for debris-flow deposition and deposit characteristics. J Sediment Res 70(1):64–83

Major JJ, Iverson RM (1999) Debris-flow deposition: effects of pore-fluid pressure and friction concentrated at flow margins. GSA Bull 111(10):1424–1434

Mangeney-Castelnau A, Vilotte JP, Bristeau MO, Perthame B, Bouchut F, Simeoni C, Yerneni S (2003) Numerical modeling of avalanches based on Saint-Venant equations using a kinetic scheme. J Geophys Res 108(B11):1–18

McDougall S, Hungr O (2005) Dynamic modelling of entrainment in rapid landslides. Can Geotech J 42:1437–1488

Medina V, Hurlimann M, Bateman A (2007) Application of FLATModel, a 2D finite volume code, to debris flows in the northern-eastern part of the Iberian peninsula. Landslides 5:127–142

O'Brien JS, Julien PY (1985) Physical properties and mechanics of hyperconcentrated sediment flows. In DS Bowles (ed) Proceedings ASCE Speciality, Conference on the delineation of landslides, flashflood, and debris flows hazards in Utah. Logan, Utah, pp 260–279

O'Brien JS, Julien PY, Fullerton WT (1993) Two-dimensional water flood and mudflow simulation. J Hydraul Eng ASCE 119(2):244–261

O'Brien JS (1986) Physical processes, rheology and modeling of mudflows. PhD thesis, Colorado State University, Fort Collins, Colorado

Paik J (2014) A high resolution finite volume for 1D debris flow. J Hydroenviron Res xx:1–11

Paik J, Park S-D (2011) Numerical simulation of flood and debris flows through drainage culvert. Ital J Eng Geol Environ Book 11:487–493

Papa M, Pianese D (2002) Influence of cross-sectional velocity, density and pressure gradients on debris flow modelling. Phys Chem Earth 27(36):1545–1550

Pastor M, Haddad B, Sorbino G, Cuomo S, Drempetic V (2009) A depth integrated coupled SPH model for flow-like landslides and related phenomena. Int J Numer Anal Methods Geomech 33(2):143–172

Pianese D (1993) Influenza della non stazionarietà e non uniformità del trasporto solido sui processi di evoluzione d'alveo, Communication No. 725. Department of Hydraulic and Environmental Engineering G. Ippolito, University of Napoli Federico II, Napoli

Pianese D (1994) Comparison of different mathematical models for river dynamics analysis. Communication No. 782. Department of Hydraulic and Environmental Engineering G. Ippolito, University of Napoli Federico II, Napoli. Presented at International Workshop on Floods and Inundations related to Large Earth Movements, Trent Univ., Trent, Italy, 4–7 Oct

Pianese D (1999) Sulle cause meteoriche di innesco dei movimenti franosi. Atti del Convegno "Analisi del dissesto idrogeologico in Italia"—Internal. Rep. no. 870. Department of Hydraulic and Environmental Engineering. Federico II University

Pianese D, Barbiero L (2003) Formulation of a two-dimensional unsteady debris-flow model for the analysis of debris-flow hazards and countermeasures thereof. In Proceedings of 3rd international conference on debris-flow hazards and mitigation: mechanics, predictions and assessment, Congress Center, Davos (Switzerland), September 10–12, 2003, vol 1, pp 705–716

Pianese D, Barbiero L (2004) Discussion of the paper: 'Case Study: Malpasset Dam-Break Simulation using a Two-Dimensional Finite Volume Method' (2002) by Alessandro Valiani, Valerio Caleffi, and Andrea Zanni, published on the J Hydraul Eng ASCE 130(9): 941-944; ISSN: 0733-9429

Potter D (1972) Computational physics. Wiley, London

Pudasaini SP, Wang Y, Hutter K (2005) Modelling debris flows down general channels. EGU NHESS 5:799–819

Quan Luna B, Remaitre A, van Asch ThWJ, Malet J-P, van Westen CJ (2011) Analysis of debris flow behavior with a one dimensional run-out model incorporating entrainment. Eng Geol 128(2012):63–75

Rossi F, Villani P (1995) Valutazione delle Piene in Campania. CNR-GNDCI, Pubbl. N. 1472, Grafica Metelliana & C., Cava de' Tirreni (SA)

Savage SB, Hutter K (1989) The motion of a finite mass of granular material down a rough incline. J Fluid Mech 199:177–215

Savage SB, Hutter K (1991) The dynamics of avalanches of granular materials from initiation to runout, part I. Analysis. Acta Mech 86:201–223

SCS (Soil Conservation Service) (1972) SCS national engineering handbook, Sec. 4. Hydrology, USDA, USA

Sosio R, Crosta GB, Frattini P (2007) Field observations, rheological testing and numerical modelling of a debris-flow event. Earth Surf Process Landf 32:290–306

Spinewine B, Zech Y (2007) Small-scale laboratory dam-break waves on movable beds. J Hydraul Res 45(Extra Issue):73–86

Takahashi T (1991) Debris flow. IAHR monograph. A.A. Balkema, Rotterdam

Takahashi T (2007) Debris flow. Mechanics, prediction and countermeasures. Taylor and Francis, Leiden

Takahashi T, Nakagawa H (1989) Debris flow hazard zone mapping. In: Proceedings Japan–China (Taipei) joint seminar on natural hazard mitigation. Kyoto, Japan, pp 363–372

Takahashi T, Tsujimoto H (1985) Delineation of the debris flow hazardous zone by a numerical simulation method. In Proceedings international syrup on erosion, debris flow and disaster prevention. Tsukuba, Japan, pp 457–462

Tarolli P, Borga M, Dalla Fontana G (2008) Analyzing the influence of upslope bedrock outcrops on shallow landsliding. Geomorphology 93:186–200

Toro EF (1999) Riemann solvers and numerical methods for fluid dynamics. Springer, Berlin

Toro EF (2001) Shock-capturing methods for free-surface shallow flows. Wiley, LTD

Toro EF, Spruce M, Speares W (1994) Restoration of the contact surface in the HLL Riemann solver. Shock Waves 4(1):25–34

Wang FW, Sassa K, Fukuoka H (2003) Downslope volume enlargement of a debris slide-debris flow in the 1999 Hiroshima, Japan, rainstorm. Eng Geol 69:309–330

Zienkiewicz OC, Chang CT, Bettess P (1980) Drained, undrained, consolidating dynamic behaviour assumptions in soils. Geotechnique 30:385–395

Zienkiewicz OC, Chan AHC, Pastor M, Shrefler BA, Shiomi T (1999) Computational geomechanics. Wiley, New York